He^{2+} transport in the Martian upper atmosphere with an induced magnetic field

V. I. Shematovich,[1] D. V. Bisikalo,[1] G. Stenberg,[2] S. Barabash,[2] C. Diéval,[2,3] and J.-C. Gérard[4]

[1] Solar wind helium may be a significant source of neutral helium in the Martian atmosphere. The precipitating particles also transfer mass, energy, and momentum. To investigate the transport of He^{2+} in the upper atmosphere of Mars, we have applied the direct simulation Monte Carlo method to solve the kinetic equation. We calculate the upward He, He$^+$, and He^{2+} fluxes, resulting from energy spectra of the downgoing He^{2+} observed below 500 km altitude by the Analyzer of Space Plasmas and Energetic Atoms 3 instrument onboard Mars Express. The particle flux of the downward moving He^{2+} ions was 1–$2 \times 10^6 \, \mathrm{cm^{-2} \, s^{-1}}$, and the energy flux is equal to 9–$10 \times 10^{-3} \, \mathrm{erg \, cm^{-2} \, s^{-1}}$. The calculations of the upward flux have been made for the Martian atmosphere during solar minimum. It was found, that if the induced magnetic field is not introduced in the simulations the precipitating He^{2+} ions are not backscattered at all by the Martian upper atmosphere. If we include a 20 nT horizontal magnetic field, a typical field measured by Mars Global Surveyor in the altitude range of 85–500 km, we find that up to 30%–40% of the energy flux of the precipitating He^{2+} ions is backscattered depending on the velocity distribution of the precipitating particles. We thus conclude that the induced magnetic field plays a crucial role in the transport of charged particles in the upper atmosphere of Mars and, therefore, that it determines the energy deposition of the solar wind.

Citation: Shematovich, V. I., D. V. Bisikalo, G. Stenberg, S. Barabash, C. Diéval, and J.-C. Gérard (2013), He^{2+} transport in the Martian upper atmosphere with an induced magnetic field, *J. Geophys. Res. Space Physics*, *118*, 1231–1242, doi:10.1002/jgra.50184.

1. Introduction

[2] Mars is immersed in the magnetized, supersonic solar wind flow and as a response induced currents are set up in the Martian ionosphere. The currents result in magnetic fields deviating from the solar wind. A void in the solar wind is created—the induced magnetosphere. The interplanetary magnetic field lines pile up and drape around this obstacle. A bow shock is also formed, which enable the solar wind flow to slow down from supersonic to subsonic velocities [e.g., *Nagy et al.*, 2004]. The boundary between the (shocked) solar wind and the induced magnetosphere, often referred to as the induced magnetosphere boundary (IMB), is, however, not completely closed. The gyroradii of the solar wind particles are large enough, compared to the size of the IMB, to enable the particles to gyrate through the piled up magnetic field and directly interact with the Martian upper atmosphere. This unique property of the small Martian induced magnetosphere allowing solar wind protons and alpha-particles assimilation in the Martian atmosphere represents an important source of some atmospheric species.

[3] There are two principal reasons to investigate the transport of helium through the induced magnetosphere. First, precipitating solar wind particles may transfer mass, energy, and momentum to the Martian upper atmosphere. Second, solar wind He^{2+} is likely a significant source of neutral helium in the atmosphere and a detailed knowledge of the helium transport to and from the Martian atmosphere is the key for understanding the evolution of Mars. Radioactive decay of uranium and thorium in the interior of the planet leads to the formation of ^{4}He, which slowly outgasses to the atmosphere. On Earth the outgassing of helium is balanced by a continuous loss of atmospheric helium due to photoionization and electron impact ionization followed by escape from the cusp region ("polar wind") [*Krasnopolsky et al.*, 1993]. The situation could be expected to be similar on Mars. However, comparing the spectroscopic observations of neutral helium made by the Extreme Ultraviolet Explorer (EUVE) satellite [*Krasnopolsky et al.*, 1994] with the observations of escaping He$^+$ made by the PHOBOS-2 spacecraft [*Barabash and Norberg*, 1994; *Barabash et al.*, 1995] lead to the conclusion that the production of helium

[1]Institute of Astronomy, Russian Academy of Sciences, Moscow, Russian Federation.
[2]Swedish Institute of Space Physics, Kiruna, Sweden.
[3]Division of Space Technology, Department of Computer Science, Electrical and Space Engineering, Luleå University of Technology, Kiruna, Sweden.
[4]LPAP, Université de Liège, Liège, Belgium.

Corresponding author: V. I. Shematovich, Institute of astronomy, Russian Academy of Science, Moscow, Russian Federation. (shematov@inasan.ru)

does not balance the loss. An additional source of helium is needed and currently solar wind He^{2+} is believed to be the main source of the Martian neutral helium [*Krasnopolsky and Gladstone*, 2005], constituting 90% of the total production. Recent studies using data from Mars Express strengthen this picture. Solar wind He^{2+} is regularly observed deep inside the Martian ionosphere [*Stenberg et al.*, 2011] and it is likely that a substantial part of it is neutralized and captured in the atmosphere. Ultimately, a quantitative understanding of the helium balance will improve the estimates of the uranium and thorium abundances and put constraints on the differentiation process in the primordial nebula.

[4] Observations are sparse. The mixing ratio of neutral helium in the Martian atmosphere is obtained from spectroscopic observations of the helium line at 584 Å [*Krasnopolsky and Gladstone*, 2005]. Evidence of solar wind penetration of the IMB is reported in a few papers [*Lundin et al.*, 2004; *Stenberg et al.*, 2011; *Diéval et al.*, 2012], but no quantitative analysis of the average net precipitation has yet been presented. The estimate of escaping He$^+$ from the atmosphere is still based on the observations by PHOBOS-2 made during solar maximum only [*Barabash et al.*, 1995].

[5] Precipitation of solar wind particles has also been studied with computer models [e.g., *Brecht*, 1997; *Kallio and Barabash*, 2001; *Modolo et al.*, 2005]. *Chanteur et al.* [2009] focused especially on the entry of solar wind He^{2+}. They showed that approximately 30% of the He^{2+} flux through an area corresponding to the cross-section of the planet is removed from the solar wind due to charge exchange into either He$^+$ or neutral He atoms. A substantial part of the created neutrals eventually impacts the exobase and are considered captured in the atmosphere. The deposition rate of neutral helium is estimated to be about $1.5 \times 10^{23}\,\text{s}^{-1}$. The ultimate fate of the He$^+$ ions is not discussed further and it is just assumed that all precipitating helium assimilates in the atmosphere. In this paper, we address the issue how the precipitating He^{2+} interacts with the Martian atmosphere.
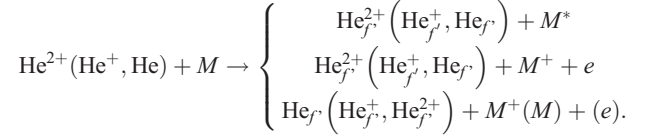
[6] To investigate the He^{2+} transport through the upper Martian atmosphere, we used the direct simulation Monte Carlo (DSMC) model [*Shematovich et al.*, 2011] and measurements of He^{2+} inside the induced magnetosphere by the ASPERA-3 experiment (Analyzer of Space Plasmas and Energetic Atoms) onboard Mars Express [*Barabash et al.*, 2006]). The main features of the model are discussed in sections 2 and 3 including a comprehensive review of the available cross-sections for the relevant processes. In section 4, results of simulations are presented. Section 5 summarizes the results and the conclusions.

2. The Model Description

2.1. He^{2+} Precipitation

[7] Interactions of precipitating energetic He^{2+} ions with the main atmospheric constituents include the momentum and energy transfer in elastic and inelastic collisions, ionization of target atmospheric molecules/atoms, charge transfer, and electron capture collisions. Energetic He atoms and He$^+$ ions produced by He^{2+} ion impacts further collide with the main atmosphere constituents, transferring their momentum and kinetic energy to atmospheric particles by elastic and inelastic collisions, ionization, and stripping processes. The

collisional processes describing the penetration of the energetic He^{2+}/He$^+$/He through the ambient atmospheric gas can be written as

$$\text{He}^{2+}(\text{He}^+, \text{He}) + M \rightarrow \begin{cases} \text{He}^{2+}_{f'}\left(\text{He}^+_{f'}, \text{He}_{f'}\right) + M^* \\ \text{He}^{2+}_{f'}\left(\text{He}^+_{f'}, \text{He}_{f'}\right) + M^+ + e \\ \text{He}_{f'}\left(\text{He}^\pm_{f'}, \text{He}^{2+}_{f'}\right) + M^+(M) + (e). \end{cases}$$

[8] Here, M denotes the major atmospheric constituents included in the model. Secondary fast He$_f$ atoms and He$^+_{f'}$ and He$^{2+}_{f'}$ ions produced by momentum transfer and stripping reactions loop the reaction set shown above. Consequently, the interaction of the precipitating He$^{2+}_{f'}$ ions with the main neutral constituents of the thermosphere must be considered as a cascade process producing a growing set of translationally and internally excited particles M* of the ambient atmospheric gas.

2.2. Mathematical Description

[9] To analyze the penetration of energetic He/He$^+$/He^{2+} particles into the atmospheric gas, we use the kinetic Boltzmann equations [*Gérard et al.*, 2000; *Shematovich et al.*, 2011] with the collision term

$$\mathbf{v}\frac{\partial}{\partial \mathbf{r}}f_\alpha + \left(\mathbf{g} + \frac{e}{m_\alpha}\mathbf{v} \times \mathbf{B}\right)\frac{\partial}{\partial \mathbf{v}}f_\alpha = Q_\alpha(\mathbf{v}) + \sum_{M=H,H_2,He,O,N_2,CO_2}J_{\text{mt}}(f_\alpha, f_M),$$

$$\alpha = \text{He}^{2+}, \text{He}^+, \text{He}$$

(1)

where $f_\alpha(\mathbf{r},\mathbf{v})$, and $f_M(\mathbf{r},\mathbf{v})$ are the velocity distribution functions for helium atoms or ions, and components of ambient gas, respectively, e the electron charge, and m_α the helium mass. The left side of the kinetic equation describes the transport of particles in the planetary gravitational and induced magnetic fields. The right-hand side term Q_α is the production rate of respective particles in charge-exchange and stripping collisions. The elastic and inelastic scattering terms J_{mt} for He/He$^+$/He^{2+} collisions with the ambient atmospheric species are written in the standard form [*Shematovich et al.*, 1994]. It is assumed that the ambient atmospheric gas is characterized by local Maxwellian velocity distribution functions.

2.3. Stochastic Approach

[10] The DSMC method used to solve the kinetic equation (1) implies generation of a sample of paths for the state of the physical system under study—He/He$^+$/He^{2+} thermalization and transport in the transition region of the upper atmosphere. It is an efficient tool for studying such complex kinetic systems in the stochastic approximation [*Shematovich et al.*, 1994; *Bisikalo et al.*, 1995; *Gérard et al.*, 2000; *Shematovich et al.*, 2011]. The details of the algorithmic realization of this numeric model were given earlier [*Shematovich et al.*, 1994; *Bisikalo et al.*, 1995]. The statistics in the DSMC model is controlled using the standard procedures [*Shematovich*, 2008]. When the steady state is reached then it is possible to accumulate the statistics with the needed accuracy. In the calculations presented below the fluxes and other characteristics were calculated with the variation below 10%. The low-energy parts of He/He$^+$/He^{2+} fluxes were calculated with the sufficient accuracy because these particles were

slowed down due to the wealth of collisions with the ambient atmospheric gas. The energy deposition rate of He/He$^+$/He^{2+} flux is determined by the cross-sections of the collisions with the ambient gas. The key point of this model is the stochastic treatment of the scattering angle distribution. This distribution influences both the energy degradation rate through the loss of energy in the momentum transfer collisions that is proportional to the sine of the scattering angle, and the angle redistribution of the precipitating He^{2+} ions.

2.4. Numerical Model

[11] We consider the He/He$^+$/He^{2+} transport between altitudes where He^{2+} ions are efficiently thermalized and atmospheric gas becomes practically collisionless. For the Martian atmosphere, the boundaries are placed at 80 and 500 km. The 80 km altitude is well below the exobase placed near 180 km at low solar activity conditions [*Fox and Hac*, 2009]. To link our model with the actual measurements, we chose the upper boundary in the altitude range below 500 km, where measurements of precipitating He^{2+} were made by the ASPERA-3 instrument. The region of the atmosphere under the study was divided into 49 vertical cells, and the altitude-dependent cell size is chosen according to the condition that it must be equal to or smaller than the free path length. In the model the radial position and three velocity components for each modeling particle are kept. The modeling particle trajectory is calculated in 3-D space for each time step and after that the new radial position is kept. Therefore, He^{2+} launched at a given angle versus nadir direction can move to different angles and planet curvature is also taken into account.

[12] The altitude distributions of the main neutral species—CO$_2$, N$_2$, O, H, H$_2$, and He—were adopted from *Fox and Hac* [2009] for a low level of solar activity corresponding to the ASPERA-3 observations. The altitude profiles of the main neutral species adopted in the model are shown in Figure 1. The temperature in the considered domain changes from 150 K at lower boundary up to 170 K at the upper boundary.

[13] The Monte Carlo code to model the penetration of high-energy protons and hydrogen atoms into the Earth's atmosphere [*Gérard et al.*, 2000] was modified to take into account the effect of the horizontal magnetic field on the ion trajectories, Martian atmosphere profiles, and respective He^{2+} interaction cross-sections. The induced magnetic field has been measured at Mars by the Mars Global Surveyor orbiter [*Brain et al.*, 2003] and the Mars Express orbiter [*Akalin et al.*, 2010]. These authors show that the induced magnetic field is mainly horizontal; its strength decreases with increasing altitude and with increasing solar zenith angle. The induced magnetic field strength is typically the strongest near the subsolar point (about 40 nT) and reaches a value of 20 nT at the terminator in the altitude range 360–440 km [*Akalin et al.*, 2010]. Following these measurements we assume the constant in time and uniform in space horizontal magnetic field $B = 10$, 20, 30, 40, and 50 nT for the different runs.

3. Compilation of Cross-Sections for He/He$^+$/He^{2+} Collisions With Atmospheric Gas

[14] In the model, the most recent measurements or calculations of the required cross-sections were adopted. We consider
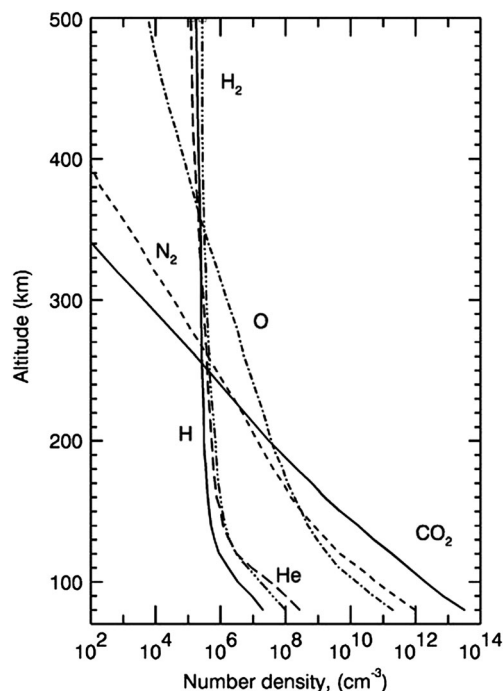

Figure 1. The altitude distributions of the main neutral species—CO$_2$, N$_2$, O, H, H$_2$, and He—adopted from *Fox and Hac* [2009].

the energy range 100 eV to 10 keV, relevant to energies of precipitating alpha-particles and include 49 reactions in the model. In general, data on the cross-sections for the interaction in this energy range are very limited and we used a number of assumptions and approximations explained in the appendix A. The compiled cross-sections for He^{2+} collisions with CO$_2$, N$_2$, O, H, H$_2$ and He are shown in Figures 2a–2f and 3, correspondingly, and summed up in Table A1.

4. Results of the Calculations

[15] The most interesting effects of solar wind He/He$^+$/He^{2+} precipitation onto the Mars upper atmosphere are heating of the neutral gas generated by momentum transfer collisions, excitation of the emissions of the ambient gas, and formation of the backscattered flux of the energetic helium atoms and ions. The latter is of particular importance because it defines the deposition rate of helium from the solar wind into the neutral atmosphere.

[16] In our simulations, we use two spectra of the downward moving He^{2+} ions, measured by the ASPERA-3 [*Barabash et al.*, 2006] on board of Mars Express for two dates: 23 January and 2 December 2005 (hereafter we call these spectra first and second, respectively). These energy spectra were observed below but close to the IMB at an altitude of about 300–500 km at a solar zenith angles of 35–40 degrees. The energy range of the ASPERA-3 instrument is 10 eV/q to 36 keV/q and, hence, covers the full energy range of interest. For the first spectrum the particle flux is equal to 1.07×10^6 cm^{-2} s^{-1}, and the energy flux is equal to 9.4×10^{-3} erg cm^{-2} s^{-1}. For the second spectrum the particle flux is equal to 1.77×10^6 cm^{-2} s^{-1}, and the energy flux is equal to 9.9×10^{-3} erg cm^{-2} s^{-1}. The energy spectra of the
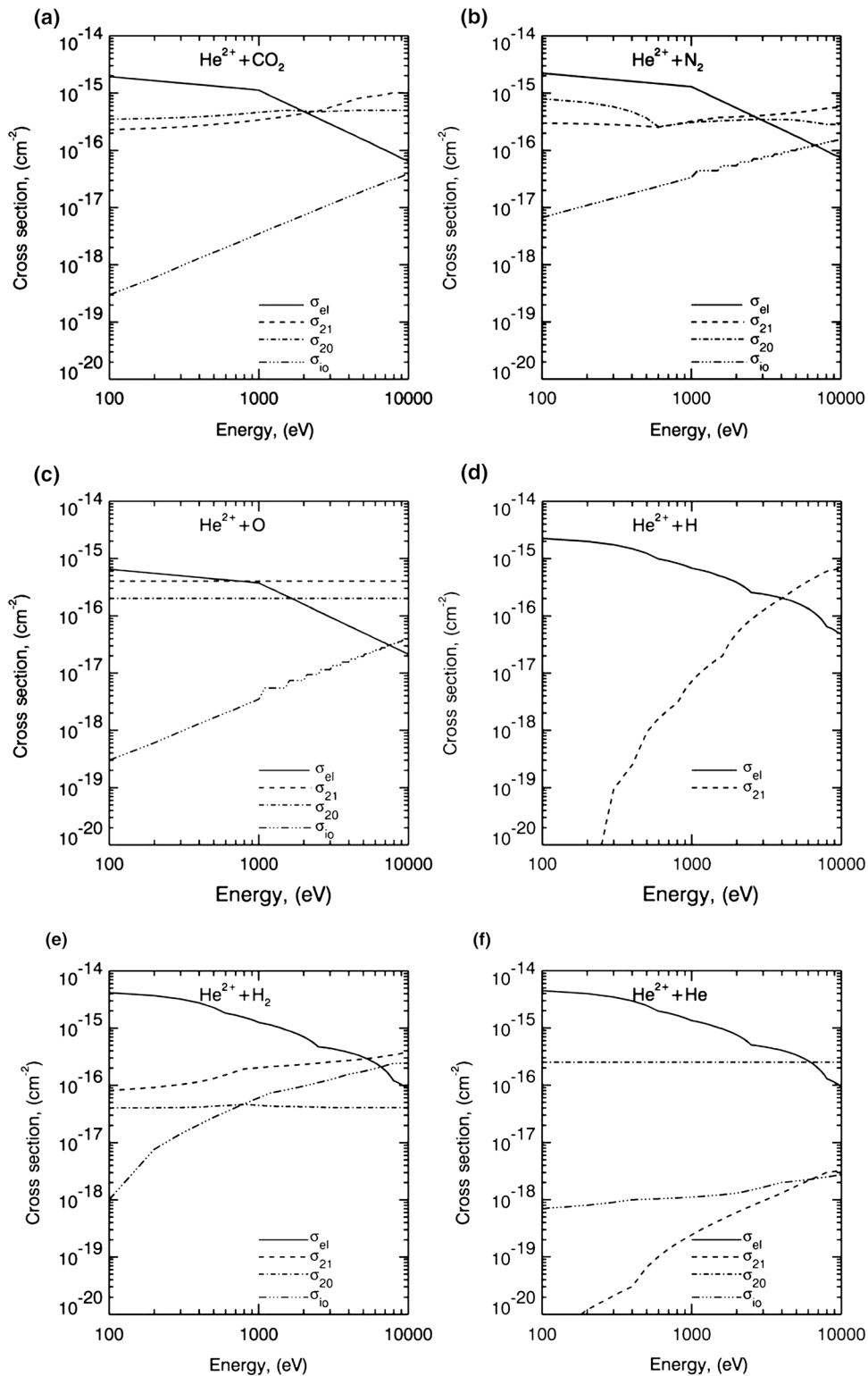
Figure 2. (a) Compilation of cross-sections for He^{2+} elastic (el), one-electron (21), two-electron (20) charge transfer, and ionization (io) collisions with CO$_2$. (b) Compilation of cross-sections for He^{2+} elastic (el), one-electron (21), two-electron (20) charge transfer, and ionization (io) collisions with N$_2$. (c) Compilation of cross-sections for He^{2+} elastic (el), one-electron (21), two-electron (20) charge transfer, and ionization (io) collisions with O. (d) Compilation of cross-sections for He^{2+} elastic (el) and one-electron (21) collisions with H. The two-electron (20) charge transfer, and ionization (io) collisions are neglected. (e) Compilation of cross-sections for He^{2+} elastic (el), one-electron (21), two-electron (20) charge transfer, and ionization (io) collisions with H$_2$. (f) Compilation of cross-sections for He^{2+} elastic (el), one-electron (21), two-electron (20) charge transfer, and ionization (io) collisions with He.
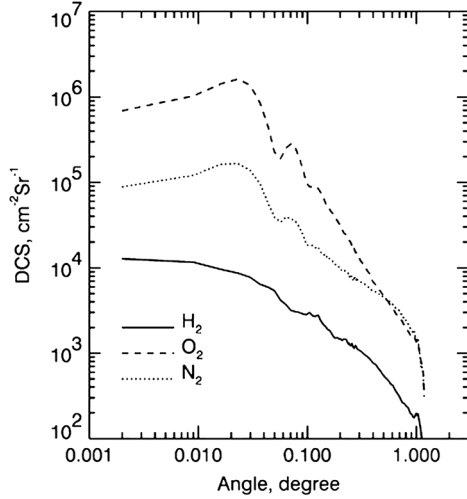
Figure 3. Scattering angle distributions in the elastic collisions of He^{2+} with H$_2$, N$_2$, and O$_2$ at a collision energy of 500 eV.
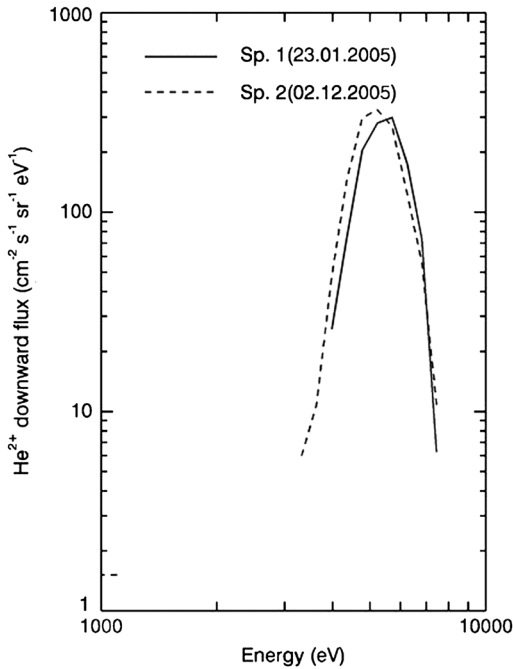

Figure 4. Energy spectra of the downward moving He^{2+} ions measured by ASPERA-3 at an altitude of 500 km for the dates 23.01.2005 and 02.12.2005.

downward moving He^{2+} ions measured by ASPERA-3 are shown in Figure 4. The He^{2+} energy spectra measured below the IMB are usually narrower in energy than those observed in the magnetosheath but with an average energy comparable to solar wind energies. The downgoing He^{2+} ions are frequently observed with most of the flux concentrated in a certain direction. Consequently, we use a monodirectional beam to model the typical distribution in our simulations.

[17] We have conducted six runs that are listed in Table 1 to estimate the magnitudes of the He^{2+}, He$^+$, and He fluxes backscattered from the Martian atmosphere. Runs 1, 2, and 3 were conducted for the first spectrum for an incident flux

Table 1. Input Data for the DSMC Model

Run #	B, Horiz., nT	Precipitating He^{2+} Distribution Versus Nadir	Precipitating Spectrum
1	20	Monodirectional 45°	ASPERA-3 (spectrum 1)
2	20	Monodirectional 60°	ASPERA-3 (spectrum 1)
3	20	Monodirectional 75°	ASPERA-3 (spectrum 1)
4	0	Monodirectional 45°	ASPERA-3 (spectrum 1)
5	40	Monodirectional 45°	ASPERA-3 (spectrum 1)
6	20	Monodirectional 45°	ASPERA-3 (spectrum 2)

with different angles of He^{2+} flux relative to nadir: 45°, 60°, and 75°, in the presence of an induced magnetic field of strength 20 nT. Runs 1, 4, and 5 allow us to evaluate the influence of the induced magnetic field ($B = 0$, 20, and 40 nT) on the solution, using the first spectrum at 45° relative to nadir. Run 6 was made with the same parameters as Run 1, but for the second spectrum.

4.1. Runs With Different Angles of He^{2+} Flux Relative to Nadir

[18] Run 1 (Table 1) was conducted for the monodirectional incident flux with an angle to nadir of 45°. The calculated energy spectra of the He^{2+}, He$^+$, and He moving upward at the model upper boundary 500 km are plotted in Figure 5a. In the calculations with the DSMC model it was found that the interaction of the precipitating He^{2+} with the upper atmosphere results in the formation of the following upward moving fluxes: for He^{2+} the particle flux is equal to $3.1 \times 10^5 \, \text{cm}^{-2} \, \text{s}^{-1}$ and the energy flux is equal to $2.7 \times 10^{-3} \, \text{erg} \, \text{cm}^{-2} \, \text{s}^{-1}$; for He$^+$, $1.7 \times 10^4 \, \text{cm}^{-2} \, \text{s}^{-1}$ and $1.5 \times 10^{-4} \, \text{erg} \, \text{cm}^{-2} \, \text{s}^{-1}$; for He, $9.5 \times 10^3 \, \text{cm}^{-2} \, \text{s}^{-1}$ and $5.9 \times 10^{-5} \, \text{erg} \, \text{cm}^{-2} \, \text{s}^{-1}$. In this case 29.2% of the particle flux and 29.1% of the energy flux of the precipitating He^{2+} are backscattered as upward moving α-particles by the Martian upper atmosphere (see Tables 2a and 2b). For He$^+$ and He the upward particle fluxes are 1.6% and 0.9%, and the energy fluxes are 1.6% and 0.6%, respectively. The energy spectrum of the upgoing He^{2+} ions follows well the spectrum of the precipitating α-particles, because of the ion gyromotion in the induced magnetic field. In total, $29.2 + 1.6 + 0.9 = 31.7\%$ of the precipitating particles are reflected backwards. The ion sensor of ASPERA-3 instrument has a limited field of view ($\pm 45 \times 360°$) and do not capture the full ion distribution at any given time. Therefore, we cannot directly compare the backscattered fluxes of He^{2+} and He$^+$ with observations. We note, however, that Mars Express regularly observes upgoing He^{2+} fluxes. These fluxes are often almost as big as the reported precipitating fluxes [*Stenberg et al.*, 2011], supporting the results obtained by the model. We also note that very little He$^+$ at solar wind energies is seen with Mars Express. To quantify and compare ratios of upgoing and downgoing He^{2+} and He$^+$ fluxes, we need to apply statistical methods to the observational data, which will be the subject of a separate paper (Stenberg et al., 2013, in preparation).

[19] Run 2 (Table 1) was conducted for the monodirectional incident flux with an angle to nadir of 60°. The calculated energy spectra of the He^{2+}, He$^+$, and He moving upward at the model upper boundary 500 km are shown in Figure 5b. The following values of upward moving fluxes were calculated: for He^{2+} the particle flux is equal to $2.5 \times 10^5 \, \text{cm}^{-2} \, \text{s}^{-1}$ and the energy flux is equal to $2.2 \times 10^{-3} \, \text{erg} \, \text{cm}^{-2} \, \text{s}^{-1}$; for He$^+$, $8.8 \times 10^3 \, \text{cm}^{-2} \, \text{s}^{-1}$ and $7.7 \times 10^{-5} \, \text{erg} \, \text{cm}^{-2} \, \text{s}^{-1}$; for He,
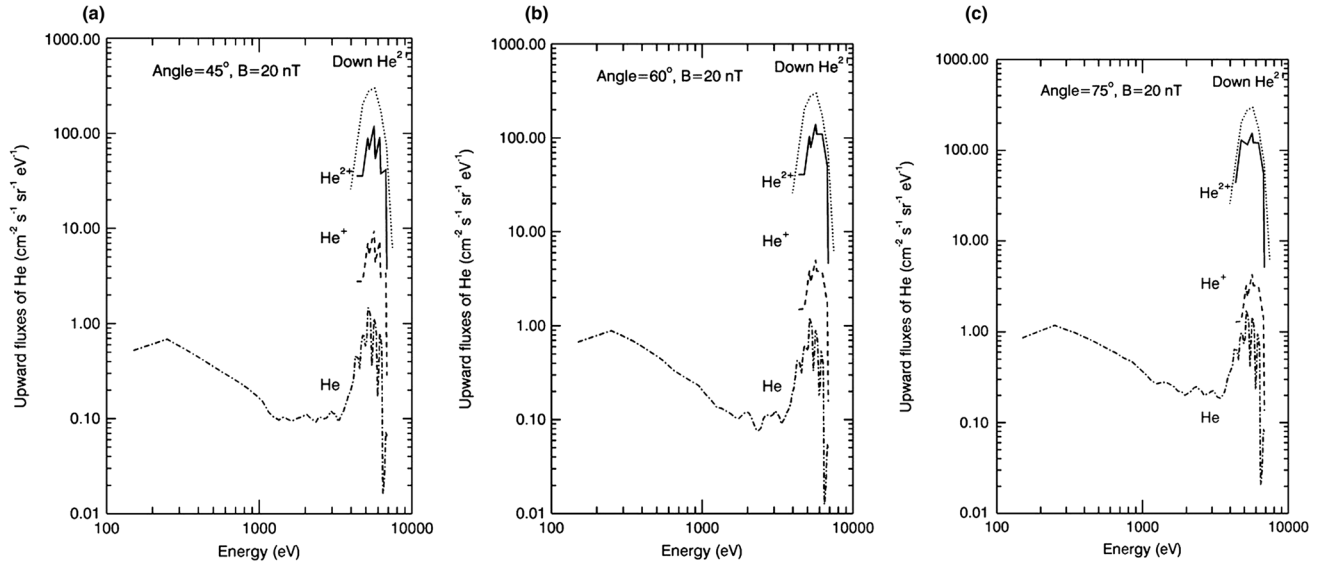
Figure 5. (a) Energy spectra of the downward (spectrum 1 marked by dotted line) and upward moving He^{2+} (solid line), He^{+} (dashed line), and He (dashed-dotted line) for the run with induced magnetic field $B = 20$ nT and with direction angle of 45° versus nadir. (b) The same as in Figure 5a for the direction angle of 60° versus nadir. (c) The same as in Figure 5a for the direction angle of 75° versus nadir.

Table 2a. Calculated Values of the Backscattered Energy Fluxes of He/He^{+}/He^{2+}

Run #	B, Horiz., nT	Precipitating He^{2+} Distribution Versus Nadir	Energy Up, He, %	Energy Up, He^{+}, %	Energy Up, He^{2+}, %	Energy up, Total, %
1	20	Monodirectional 45° (spectrum 1)	0.6	1.6	29.1	31.3
2	20	Monodirectional 60° (spectrum 1)	0.7	1.2	33.2	35.1
3	20	Monodirectional 75° (spectrum 1)	2.2	1.8	35.6	39.6
4	0	Monodirectional 45° (spectrum 1)	0.0	0.0	0.0	0.0
5	40	Monodirectional 45° (spectrum 1)	0.4	14.3	50.7	65.4
6	20	Monodirectional 45° (spectrum 2)	0.7	1.9	29.4	32.0

Table 2b. Calculated Values of the Backscattered Particle Fluxes of He/He^{+}/He^{2+}

Run #	B, Horiz., nT	Precipitating He^{2+} Distribution Versus Nadir	Particles Up, He, %	Particles Up, He^{+}, %	Particles Up, He^{2+}, %	Particles Up, Total, %
1	20	Monodirectional 45° (spectrum 1)	0.9	1.6	29.2	31.7
2	20	Monodirectional 60° (spectrum 1)	1.2	1.2	33.3	35.7
3	20	Monodirectional 75° (spectrum 1)	3.5	1.8	35.6	40.9
4	0	Monodirectional 45° (spectrum 1)	0.0	0.0	0.0	0.0
5	40	Monodirectional 45° (spectrum 1)	0.5	14.3	50.9	65.7
6	20	Monodirectional 45° (spectrum 2)	0.9	2.0	29.6	32.5

9.0×10^{3} cm^{-2} s^{-1} and 4.8×10^{-5} erg cm^{-2} s^{-1}. To calculate the relative values of the upward flux, one must take into account that for the monodirectional case the incident flux becomes smaller as the angle to nadir θ increases (as cos(θ)). In this case for He^{2+}, He^{+}, and He the upward particle fluxes are 33.3%, 1.2%, and 1.2%, and the energy fluxes are 33.2%, 1.2%, and 0.7%, respectively (see Tables 2a and 2b). In total, $33.3 + 1.2 + 1.2 = 35.7\%$ of the precipitating particles are reflected backward.

[20] Run 3 (Table 1) was conducted for a monodirectional incident flux with an angle to nadir of 75°. The calculated energy spectra of the He^{2+}, He^{+}, and He moving upward at the model upper boundary at 500 km altitude are given in Figure 5c. The value of the upward moving fluxes is 1.4×10^{5} cm^{-2} s^{-1} for He^{2+} ions and the energy flux is 1.2×10^{-3} erg cm^{-2} s^{-1}; for He^{+}, 7.1×10^{3} cm^{-2} s^{-1} and 6.2×10^{-5} erg cm^{-2} s^{-1}; for He, 1.4×10^{4} cm^{-2} s^{-1} and 7.5×10^{-5} erg cm^{-2} s^{-1}. In this case of He^{2+}, He^{+}, and He the upward particle fluxes are 35.6%, 1.8%, and 3.5%, and the energy fluxes are 35.6%, 1.8%, and 2.2%, respectively (see Tables 2a and 2b). In total, $35.6 + 1.8 + 3.5 = 40.9\%$ of the precipitating particles are backscattered. In Figures 5a–5c it is seen that low-energy fraction of the upward flux is formed for helium atoms only. Analysis of the data given in Figures 2a–2c shows that the one- and two-electron charge exchange cross-sections for He^{2+} and He^{+} ions exceed the

elastic cross-sections at energies above 1 keV. Therefore, He^{2+} and He$^+$ ions can successfully capture electrons in the very first collisions with the main atmospheric species. Consequently, the fresh helium atoms with the relatively high kinetic energies can penetrate deep into the atmosphere, where the low energy fraction of upward-moving He atoms is formed mainly due to the momentum transfer in the collisions with the main atmospheric species.

4.2. Runs With the Induced Magnetic Field

[21] For the incident α-particles spectrum 1, and for a monodirectional flux with angle value of 45°, we have conducted three runs for $B = 0$, 20, and 40 nT (Runs 4, 1, and 5 from Table 1). Calculations for the nonmagnetic case show that there are no upward fluxes. For the case of $B = 20$ nT the values of the backscattered (upward) particle and energy fluxes were given in the description of Run 1. For the case of $B = 40$ nT we have obtained the following estimates of the backscattered (upward) particle and energy fluxes (see Figure 6): for He^{2+} the particle flux is 5.4×10^5 cm^{-2} s^{-1} and the energy flux is 4.8×10^{-3} erg cm^{-2} s^{-1}; for He$^+$, 1.5×10^5 cm^{-2} s^{-1} and 1.3×10^{-3} erg cm^{-2} s^{-1}; and for He, 5.2×10^3 cm^{-2} s^{-1} and 3.5×10^{-5} erg cm^{-2} s^{-1}. For He^{2+}, He$^+$, and He the upward particle fluxes are 50.9%, 14.3%, and 0.5%, and energy fluxes are 50.7%, 14.3%, and 0.4%, respectively (see Tables 2a and 2b). In total, $50.9 + 14.3 + 0.5 = 65.7\%$ of the precipitating particles are reflected backward.

[22] For the incident He^{2+} spectrum 2, we have conducted the run (Run 6 from the Table 1) with a typical value of the horizontal component of the induced magnetic field $B = 20$

nT, and with angle to nadir of 45°. We obtained the following estimates of the relative backscattered (upward) particle and energy fluxes (see Figure 7): for He^{2+} the particle flux is 3.5×10^5 cm^{-2} s^{-1} and the energy flux is 2.9×10^{-3} erg cm^{-2} s^{-1}; for He$^+$, 2.3×10^4 cm^{-2} s^{-1} and 1.9×10^{-4} erg cm^{-2} s^{-1}; and for He, 1.1×10^4 cm^{-2} s^{-1} and 6.4×10^{-5} erg cm^{-2} s^{-1}. For He^{2+}, He$^+$, and He the upward energy fluxes are 29.4%, 1.9%, and 0.7%, and particle fluxes are 29.6%, 2.0%, and 0.9%, respectively (see Tables 2a and 2b). In total, $29.6 + 2.0 + 0.9 = 32.5\%$ of the precipitating particles are reflected backward. The particle and energy fluxes of backscattered He/He$^+$/He^{2+} of solar wind origin are summarized in Tables 2a and 2b, correspondingly.

[23] We have conducted a set of sensitivity runs to estimate the influence of the assumptions on the cross-sections for several reactions for which no data were available. Such runs were conducted for the reference case (Run 1) but the cross-sections under sensitivity study were enlarged and reduced by a factor of 2. Namely, we have conducted the sensitivity runs for the following sets of cross-sections: (i) for elastic collisions between He$^+$ ions and the main atmospheric species CO_2, N_2, and O (processes 1.7–1.11 in Table A1), the cross-sections were assumed to be equal to the ones for respective collisions between He^{2+} ions and CO_2, N_2, and O; (ii) for one-electron charge exchange collisions He$^+$ + CO_2, N_2, O (processes 2.7–2.10 in Table A1) the cross-sections were suggested to be based on the cross-sections for the one-electron charge exchange collisions He^{2+} + CO_2, N_2, O but normalized by the respective factors to match the measured cross-sections for He$^+$ + CO_2, N_2 collisions at energy of 0.5 keV [*Gao et al.*, 1990]; (iii) for
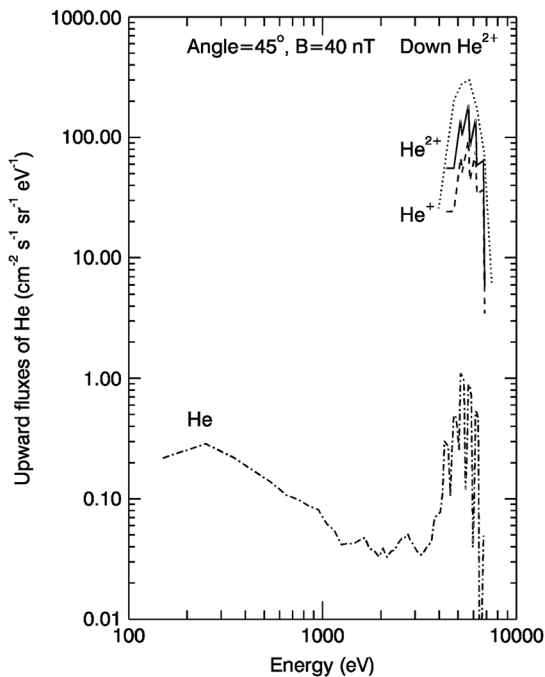

Figure 6. Energy spectra of the downward (spectrum 1 marked by dotted line) and upward moving He^{2+} (solid line), He$^+$ (dashed line), and He (dashed-dotted line) for the run for spectrum 1 with the 40 nT horizontal component of the induced magnetic field and with direction angle of 45° versus nadir.
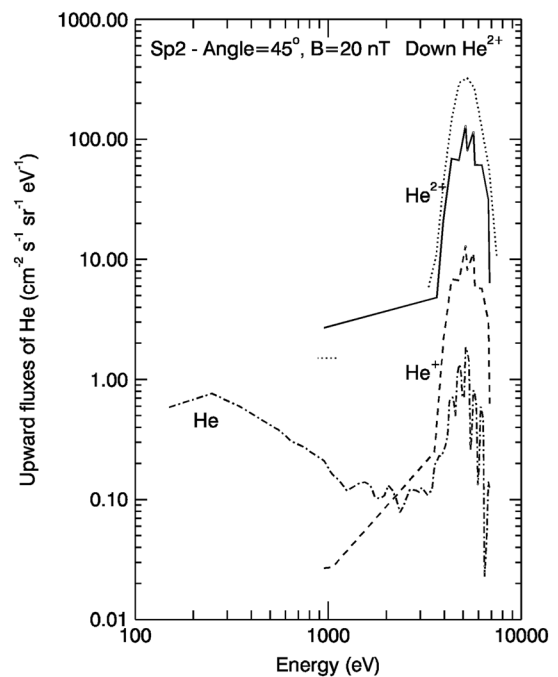

Figure 7. Results of calculations for incident spectrum 2 (03.12.2005). Energy spectra of the downward (dotted line) and upward moving He^{2+} (solid line), He$^+$ (dashed line), and He (dash-dotted line) for the run with the 20 nT horizontal component of the induced magnetic field and with direction angle of 45° versus nadir.

ionization collisions He^{2+} + CO$_2$, N$_2$, O (processes 4.1–4.3 in Table A1) the cross-sections were suggested to be based on the cross-sections for the ionization collisions between protons and the main atmospheric species—CO$_2$, N$_2$, O— taken from the compilation by *Haider et al.* [2002], with the scaling factors indicated in Table A1.

[24] We have conducted two sensitivity runs for each group of processes (i)–(iii) when the cross-sections of the reactions under study were enlarged and reduced by a factor of 2. We found that the upward flux of He^{2+} ions was changed by 0.5% for group (i) of elastic collisions, by 3.5% for group (ii) of one-electron charge exchange collisions, and by 1.5% for group (iii) of ionization collisions relative to the value of this flux for the reference case (Run 1). Therefore, influence of the suggestions on the cross-sections under sensitivity study is below the value of 5%—the accuracy of the model.

5. Summary and Conclusions

[25] We developed a DSMC model to investigate the transport of the solar wind helium ions and atoms in the Martian upper atmosphere. The model takes into account all physical interaction processes of the He/He$^+$/He^{2+} as they travel through the atmosphere. The important features of the elaborated model are: the detailed consideration of the scattering angle in each collision and the use of the most recent set of cross-sections.

[26] We calculated the backscattered flux of energetic He/ He$^+$/He^{2+} particles and the total energy deposition rates. The calculations have been performed for the Martian atmosphere during solar minimum conditions. We use two spectra of the incident He^{2+} ions at the altitude of 500 km measured by the Mars Express ASPERA-3 instrument in the energy range 700 eV to 20 keV on 23 January and 3 December 2005. The calculated particle and energy fluxes of the incident He^{2+} ions are equal to 1.07×10^6 cm^{-2} s^{-1} and 9.4×10^{-3} erg cm^{-2} s^{-1} for the first measurement, and 1.77×10^6 cm^{-2} s^{-1} and 9.9×10^{-3} erg cm^{-2} s^{-1} for the second measurement.

[27] It was found that with increase of the angle of He^{2+} incident flux relative to nadir, the fluxes of He/He$^+$/He^{2+} particles backscattered by the Martian upper atmosphere increase. For angles of 45°, 60°, and 75°, we found that the total upward energy flux is as much as 31.3%, 35.1%, and 39.6%, respectively.

[28] The horizontal magnetic field induced by the solar wind leads to an increase of the upward He$^+$/He^{2+} flux because of the ion gyromotion. Including a 20 nT (40 nT) horizontal magnetic field in the altitude range of 85–500 km in the model gives the total backscattered flux of 31.7% (65.7%). The magnetic field thus plays a crucial role in the transport of charged particles and determines the energy deposition of the solar wind alpha-particles in the upper atmosphere of Mars. No more than 70% of all helium ions penetrating the induced magnetosphere are assimilated in the atmosphere. This does not rule out solar wind helium as an important source of atmospheric helium, but the upper atmosphere may be better protected from penetrating He^{2+} than was previously thought. The capture efficiency is at least 30% lower than one normally assumes and the helium contribution from the solar wind to the atmosphere may be smaller than has been suggested.

[29] The gyroradius of 1 keV He^{2+} ion in a 20 nT magnetic field is about 230 km, which is close the distance between the induced magnetosphere boundary and the exobase. Therefore, the majority of the ions cannot penetrate into the high neutral density region and is turned back by the Lorentz force rather than get scattered by the atmospheric neutral particles.
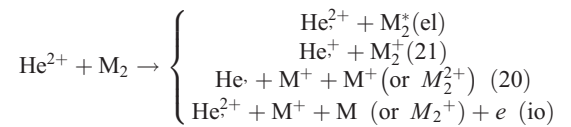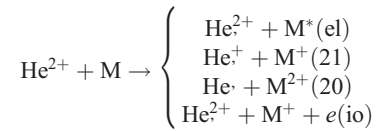
[30] The simulations with a magnetic field also show that the main component of the backscattered flux is He^{2+} ions. This somewhat unexpected result stems from the larger cross-section of elastic scattering than the sum of all processes modifying the charge state of the precipitating He^{2+} ions.

[31] It is instructive to compare the obtained results with the similar studies of the proton/hydrogen precipitation [*Shematovich et al.*, 2011]. In the case of no magnetic field the total protons and hydrogen backscattered flux is estimated to be about 22% of the impinging flux, while for He^{2+} it is less than 1%. Due to the larger mass ratio between hydrogen and the main atmospheric constituents at the exobase (O and CO$_2$) than for alpha-particles, backward scattering is more effective for hydrogen. Yet, the fraction of the neutral component relative to the original ions is larger for hydrogen due to small charge-exchange cross-sections for the He^{2+} interactions. For the runs with magnetic fields, backscattering of helium ions and atoms significantly increases (up to 31.7 and 65.7% for $B = 20$ and 40 nT, respectively). Therefore, similarly to the proton precipitation, it is the magnetic field inside the induced magnetosphere that prevents the precipitating particles from reaching the atmosphere and thus reduces the inflow of matter and energy.

Appendix A: Compilation of Cross-Sections for He/He$^+$/He^{2+} Collisions With Atmospheric Gas

A1. Cross-Sections for He^{2+} Collisions With CO$_2$, N$_2$, and O

[32] We have considered four processes for the interaction of He^{2+} with atomic (M) and molecular (M$_2$) atmospheric gas; elastic (σ_{el}), one-electron charge exchange (σ_{21}), two-electron charge exchange (σ_{20}), and ionization (σ_{io})

$$\text{He}^{2+} + \text{M} \rightarrow \begin{cases} \text{He}^{2+} + \text{M}^*\text{(el)} \\ \text{He}^+ + \text{M}^+\text{(21)} \\ \text{He}^\cdot + \text{M}^{2+}\text{(20)} \\ \text{He}^{2+} + \text{M}^+ + e\text{(io)} \end{cases}$$

$$\text{He}^{2+} + \text{M}_2 \rightarrow \begin{cases} \text{He}^{2+} + \text{M}_2^*\text{(el)} \\ \text{He}^+ + \text{M}_2^+\text{(21)} \\ \text{He}^\cdot + \text{M}^+ + \text{M}^+ \left(\text{or } M_2^{2+}\right) \ (20) \\ \text{He}^{2+} + \text{M}^+ + \text{M} \ \left(\text{or } M_2^+\right) + e \ \text{(io)} \end{cases}$$

[33] Unfortunately, the cross-sections for the elastic interactions He^{2+} + CO$_2$, N$_2$, and O are unknown. To approach these cross-sections, we used the same analytic approximations of σ_{el} as for H$^+$ + O$_2$, N$_2$, and O taken from the model of the proton aurora at Earth [*Gérard et al.*, 2000] in the energy range [100 eV to 10 keV]. The only calculation we found in the literature was cross-sections for elastic He + O collisions up to 5 eV [*Bovino et al.*, 2011]. Therefore, we normalized the analytic approximation for the elastic collisions He^{2+} + CO$_2$ to be equal to the calculated one at 1 eV, i.e., by the factor $\sigma_{el}(\text{He} + \text{O}; E = 1 \text{ eV})/\sigma_{el}(\text{H}^+ + \text{O}_2; E = 1$

eV) $= 3.8 \times 10^{-15}/3.02 \times 10^{-14} = 0.119$. After that we assume that a three-atom molecule (like CO_2) can be described by the same curve shape with cross-section values 3/2 times larger than the ones for a two-atom molecule. Furthermore, we assume that the elastic cross-section for He^{2+} + O collisions can be described by the same curve shape as one for H$^+$ + O$_2$ but the scaling factor calculated above should be reduced by a factor of 2. For the elastic collisions He^{2+} + N$_2$ the same procedure as for He^{2+}+CO$_2$ was used, but the scaling factor was evaluated from the paper by *Newman et al*. [1985]. We normalized the analytic approximation to be equal to the calculated one at 0.5 keV, i.e., by a factor of σ_{el}(He + N$_2$; E = 500 eV)/ σ_{el}(H$^+$+N$_2$;E = 500 eV) = $1.92 \times 10^{-15}/7. \times 10^{-15} = 0.274$.

[34] For the one-electron and two-electron charge exchange processes σ_{21} and σ_{20} in the collisions of He^{2+} ions with CO$_2$ and N$_2$ molecules, the cross-sections were taken from Table 2 in *Kusakabe et al*. [2006]. In case of collisions of He^{2+} ions with atomic oxygen O, the cross-section σ_{21} was taken following *Chanteur et al*. [2009], the same as the one for the process He^{2+} + O$_2$ → He$^+$ + O$^+$ +O from *Rudd et al*. [1985]. The cross-section σ_{20} for He^{2+} collisions with O was taken from *Rudd et al*. [1985]. Values of σ_{20} and σ_{21} for the interaction of He^{2+} with atomic oxygen were given at energies above 5 keV; therefore, following *Chanteur et al*. [2009], we adopt the constant values for low energies as $2. \times 10^{-16}$ cm^2 and $4. \times 10^{-16}$ cm^2, respectively.

[35] The ionization cross-section for the He^{2+} + CO$_2$ process was not found in the literature. To get σ_{io} for He^{2+} collisions with CO$_2$ molecules, we assume that it has the same shape as H$^+$+CO$_2$ in Haider's compilation of cross-sections [*Haider et al*., 2002]. We did not find even a single point to normalize this cross–section; therefore, we assume that the scaling factor is the same as for interaction with atomic oxygen. For atomic oxygen there are cross-sections for ionization by H$^+$ from compilation [*Haider et al*., 2002] and calculations of ionization by He^{2+} ions from [*Sahoo*, 2000]. Using these data we evaluated the scaling factor as 0.5 at 10 keV, and apply it to σ_{io}(H$^+$+CO$_2$) to get the approximation of the σ_{io} (He^{2+} + CO$_2$) cross-section. In case of He^{2+} + N$_2$ collisions, the cross-section σ_{io} shape was adopted from [*Haider et al*., 2002] and the scaling factor was assumed to be equal to 1. For He^{2+} + O collisions the σ_{io} shape was adopted from [*Haider et al*., 2002] and the scaling factor was taken equal to 0.5 [*Sahoo*, 2000].

A2. Cross-Sections for He^{2+} Collisions With H, H$_2$, and He

[36] We assumed that for elastic collisions of He^{2+} ions with H the shape of σ_{el} cross-section is similar to the one for the elastic collisions of protons H$^+$ with helium atoms given in *Krstic and Schultz* [2006], but to evaluate the scaling factor of $1.08 \times 10^{-15}/2.46 \times 10^{-15} = 0.439$ value, we used the measurements of elastic cross-sections for the process He + He at a collision energy of 500 eV from *Newman et al*. [1985]. For elastic collisions of He^{2+} ions with H$_2$ molecules, it was again assumed that the shape of σ_{el} cross-section is similar to the one for the elastic collisions of protons H$^+$ with helium atoms given in *Krstic and Schultz* [2006], but to evaluate the scaling factor of $9.3 \times 10^{-16}/5. \times 10^{-16} = 1.86$ value, we used the measurements of the elastic cross-sections for the process He + H$_2$ at collision

energy of 1500 eV from *Newman et al*. [1985]. A similar approximation procedure was used for elastic collisions of He^2$^+$ ions with He, but the scaling factor of $1.08 \times 10^{-15}/2.46 \times 10^{-15} = 0.439$ was used in accordance with data for He + He collisions at 0.5 keV from [*Newman et al*., 1985].

[37] For the one-electron and two-electron charge exchange processes σ_{21} and σ_{20} in the collisions of He^{2+} ions with H$_2$ molecules, the cross-sections were taken from Table 2 in *Kusakabe et al*. [2006]. In case of collisions of He^{2+} ions with hydrogen and helium atoms, the cross-sections σ_{21} were taken from *Ito et al*. [1993]. For the two-electron charge exchange process of He^{2+} collisions with He, the value σ_{20} was taken equal to 2.5×10^{-16} cm^2 [*Janev et al*., 1987; *Barnett et al*., 1990]. The cross-section σ_{20} He^{2+} + H is assumed to be negligible.

[38] The ionization cross-sections for the He^{2+} ions collisions with H, H$_2$, and He were adopted from the compilation by *Ito et al*. [1995]. It is necessary to point out that the values of σ_{io} (He^{2+} + H) at collision energies below 10 keV are less than 10^{-21} cm^2; therefore, in the model this cross-section was assumed to be equal to zero.

A3. Cross-Sections for He$^+$ Collisions With CO$_2$, N$_2$, O, H, H$_2$, and He

[39] We have considered four processes for the interaction of He$^+$ ions with atomic (M) and molecular (M$_2$) atmospheric gas: elastic (σ_{el}), charge exchange (σ_{10}), ionization (σ_{io}), and stripping (σ_{12}, i.e., He$^+$ + M → He^{2+} + M + e). Unfortunately, we did not find any laboratory or computational data on the cross-sections for elastic collisions of He$^+$ ions with the atmospheric species under study in the literature. Therefore, we assumed in the model that σ_{el} for elastic collisions between He$^+$ ions and atmospheric species are the same as ones for the He^2$^+$ ions (see the previous section). For the elastic process He$^+$ + He σ_{el} was assumed to be equal to the cross-section for the elastic process H$^+$ + He taken from *Krstic and Schultz* [2006], but to evaluate the scaling factor of $1.08 \times 10^{-15}/2.46 \times 10^{15} = 0.439$, we used the measurements of elastic cross-sections for the process He + He at the collision energy 0.5 keV from *Newman et al*. [1985].

[40] For the charge exchange collisions between He$^+$ ions and CO$_2$, N$_2$, and O species the shape of the cross-sections σ_{10} were taken the same as σ_{21} for the one-electron charge exchange processes He^{2+} + CO$_2$, N$_2$, and O, but with scaling factors adopted from *Gao et al*. [1990], where measurements at 1.5 keV were made for He$^+$ + N$_2$ and O$_2$ charge exchange collisions. The scaling factors are equal to $8.3 \times 10^{-16}/3.98 \times 10^{-16} = 2.09$ for CO$_2$, $3.7 \times 10^{-16}/3.76 \times 10^{-16} = 0.98$ for N$_2$, and $8.3 \times 10^{-16}/8.45 \times 10^{-16} = 0.98$ for O. Cross-sections for charge exchange collisions He$^+$ + H, H$_2$, He → He + H$^+$, H$_2^+$, He$^+$ were adopted from the compilation of *Ito et al*. [1993].

[41] The ionization cross-sections σ_{io} for the He$^+$ + CO$_2$ N$_2$, and O processes were not found in the literature; therefore, it was assumed in the model that these cross-sections are the same as for He^{2+} + CO$_2$, N$_2$, and O ionization processes. The ionization cross-sections σ_{io} of the He$^+$ collisions with atomic hydrogen H, molecular hydrogen H$_2$, and helium He were taken from the compilation of *Ito et al*. [1995]. It is necessary to mention that values of cross-section for the ionization process He$^+$ + H are extremely small below 10 keV.

[42] Laboratory and/or computed data on the cross-sections for stripping processes (He$^+$ + CO$_2$, N$_2$, O $\rightarrow$ He^{2+} + CO$_2$, N$_2$, O + e) were not found in the literature. Cross-sections for stripping collisions (He$^+$ + H, H$_2$, He $\rightarrow$ He^{2+} + H, H$_2$, He + e) are given in the compilation of *Ito et al.* [1995], but their values are extremely small $<10^{-20}$–10^{-21} at energies below 10 keV. Therefore, the stripping processes were not considered in the model.

A4. Cross-Sections for He Collisions With CO$_2$, N$_2$, O, H, H$_2$, and He

[43] We have considered three processes for the interaction of He atoms with atomic (M) and molecular (M$_2$) atmospheric gas: elastic (σ_{el}), ionization (σ_{io}), and stripping (σ_{01}, i.e., He + M $\rightarrow$ He$^+$ + M + e). We did not find any laboratory or computational data on the elastic and ionization cross-sections of He atoms with the atmospheric species CO$_2$, N$_2$, and O in the literature. Therefore, we assumed in the model that σ_{el} and σ_{io} for elastic and ionization collisions between He atoms and atmospheric species CO$_2$, N$_2$, and O are the same as ones for the He$^+$ ions (see the previous subsection). The cross-sections for elastic collisions He + H, and H$_2$ were assumed to be the same as for He$^+$ + H, and H$_2$ collisions. In case of elastic process He + He σ_{el} was assumed to be equal to the cross-section for the elastic process H$^+$ + He taken from *Krstic and Schultz* [2006], but to evaluate the scaling factor of $1.08 \times 10^{-15}/2.46 \times 10^{-15} = 0.439$, we used the measurements of elastic cross-sections for the process He + He at a collision energy of 0.5 keV from *Newman et al.* [1985].

[44] The ionization cross-sections σ_{io} in the He collisions with molecular hydrogen, and helium were taken from the compilation of *Ito et al.* [1995]. It is necessary to mention that values of cross-section for the ionization process He + H were not found in the literature, therefore this cross-section was equal to zero in the model.

[45] We did not find any laboratory or computed data on the cross-sections for stripping processes (He + CO$_2$, N$_2$, O He$^+$ + CO$_2$, N$_2$, O + e) in the literature; therefore, these processes were not taken into account in the model. Cross-sections for stripping collisions (He + H, H$_2$, He $\rightarrow$ He$^+$ +

H, H$_2$, He + e) were taken from the compilation of *Ito et al.* [1995]. It is necessary to mention that the measurements for stripping collisions with atomic hydrogen were made for energies above 80 keV; therefore, this cross-section was taken equal to zero in the model. For collisions with molecular hydrogen and helium there are additional channels (He + H$_2$, He $\rightarrow$ He^{2+} + H$_2$, He + 2e), but the magnitudes of the cross-sections for such channels are extremely small $<10^{-20}$–10^{-21} at energies below 10 keV.

A5. Scattering Angle Distributions for Collisional Processes

[46] Collisions of high-energy He/He$^+$/He^{2+} particles with the ambient atmospheric gas are characterized by the scattering angle distributions (SADs), which were measured in the laboratory at given energies of the projectile particles [*Lindsay and Stebbings*, 2005]. Such distributions are usually peaked at small scattering angles (see Figure 3) reducing the efficiency of energy transfer from high-energy impact particles to the target atmospheric particles.

[47] To take into account this effect, the following scattering angle distributions were used in the model:

[48] 1. For He + CO$_2$, N$_2$, and O processes, we adopted the SADs measured for elastic scattering and ionization in the high-energy He + O$_2$, N$_2$, and O$_2$ collisions [*Newman et al.*, 1985]. For stripping He + CO$_2$, N$_2$, and O $\rightarrow$ He$^+$ + . . . collisions, we did not find any data on the scattering angle distributions, therefore we used the measured SADs for He$^+$ + O$_2$, N$_2$, and O$_2$ charge transfer collisions at 1.5 keV energy [*Gao et al.*, 1990];

[49] 2. For He + H, H$_2$, and He processes, we adopted the SADs measured for elastic scattering and ionization in the high-energy He + H, H$_2$, and He collisions [*Newman et al.*, 1985]. For stripping He + H, and H$_2$ $\rightarrow$ He$^+$ + . . . collisions, we did not find any data on the scattering angle distributions; therefore, we used the measured SADs for He$^+$ + H$_2$ charge transfer collisions at 1.5 keV energy [*Gao et al.*, 1990]. For stripping He + He $\rightarrow$ He$^+$ + He + e collisions, we did not find any data on SAD; therefore, we used the SAD measured for elastic and charge transfer He$^+$ + He collisions at 1.5 keV energy [*Gao et al.*, 1988];

Table A1. Summary of Cross-Sections for the He/He$^+$/He^{2+} Impact on the Atmospheric Species

No.	Reactions	Reference	Comment / Assumptions
1. Elastic interactions: He^{2+} + M $\rightarrow$ He^{2+} + M*			
1.1	He^{2+} + CO$_2$	Not available	Based on H$^+$ + O$_2$ from *Gérard et al.* [2000] for 0.1–10 keV normalized by the factor 0.119 to match the theoretically calculated cross-section for He + O at 1 eV [*Bovino et al.*, 2011].
1.2	He^{2+} + N$_2$	Not available	Based on H$^+$ + N$_2$ from *Gérard et al.* [2000] for 0.1–10 keV normalized by the factor 0.274 to match the measured cross-section for He + N$_2$ at 500 eV [*Newman et al.*, 1985].
1.3	He^{2+} + O	Not available	Based on H$^+$ + O$_2$ from *Gérard et al.* [2000] for 0.1–10 keV normalized by the factor 0.119/2 to match the theoretically calculated cross-section for He + O at 1 eV [*Bovino et al.*, 2011].
1.4	He^{2+} + H	Not available	Based on He + H$^+$ from *Krstic and Schultz* [2006] for 0.1–10 keV normalized by the factor 0.439 to match the measured cross-section for He + H$^+$ at 0.5 keV [*Newman et al.*, 1985].
1.5	He^{2+} + H$_2$	Not available	Based on He + H$^+$ from *Krstic and Schultz* [2006] for 0.1–10 keV normalized by the factor 1.86 to match the measured cross-section for He + H$_2$ at 1.5 keV [*Newman et al.*, 1985].
1.6	He^{2+} + He	Not available	Based on He + H$^+$ from *Krstic and Schultz* [2006] for 0.1–10 keV normalized by the factor 0.439 to match the measured cross-section for He + He at 0.5 keV [*Newman et al.*, 1985].

Table A1. (continued)

No.	Reactions	Reference	Comment / Assumptions
1.7-11	He$^+$ + CO$_2$, N$_2$, O, H, H$_2$	Not available	Assumed to be equal to respective collisions for He^{2+}
1.12	He$^+$ + He	Not available	Based on He + H$^+$ from *Krstic and Schultz* [2006] for 0.1–10 keV normalized by the factor 0.439 to match the measured cross-section for He + He at 0.5 keV [*Newman et al.*, 1985].
1.13-17	He + CO$_2$, N$_2$, O, H, H$_2$	Not available	Assumed to be equal to respective collisions for He$^+$
1.18	He + He	Not available	Based on He + H$^+$ from *Krstic and Schultz* [2006] for 0.1–10 keV normalized by the factor 0.439 to match the measured cross-section for He + He at 0.5 keV [*Newman et al.*, 1985].
2. One-electron charge exchange: He^{2+} + M → He$^+$ + M$^+$			
2.1	He^{2+} + CO$_2$	[*Kusakabe et al.*, 2006]	
2.2	He^{2+} + N$_2$	[*Kusakabe et al.*, 2006]	
2.3	He^{2+} + O	[*Rudd et al.*, 1985]	In accordance to *Chanteur et al.* [2009] σ_{21} was taken equal to 4. × 10^{-16} cm^2 for $E < 5$ keV.
2.4	He^{2+} + H	[*Ito et al.*, 1993]	
2.5	He^{2+} + H$_2$	[*Kusakabe et al.*, 2006]	
2.6	He^{2+} + He	[*Ito et al.*, 1993]	
2.7-10	He$^+$ + CO$_2$, N$_2$, O	Not available	Based on He^{2+} + CO$_2$, N$_2$, O normalized by the respective factors to match the measured cross-section for He$^+$ + N$_2$, O$_2$ at 0.5 keV [*Gao et al.*, 1990].
2.11-13	He$^+$ + H, H$_2$, He	[*Ito et al.*, 1993]	
3. Two-electron charge exchange: He^{2+} + M → He + M^{++}			
3.1	He^{2+} + CO$_2$	[*Kusakabe et al.*, 2006]	
3.2	He^{2+} + N$_2$	[*Kusakabe et al.*, 2006]	
3.3	He^{2+} + O	[*Rudd et al.*, 1985]	In accordance to *Chanteur et al.* [2009] σ_{20} was taken equal to 2. × 10^{-16} cm^2 for E < 5 keV.
3.4	He^{2+} + H$_2$	[*Kusakabe et al.*, 2006]	
3.5	He^{2+} + He	[*Janev et al.*, 1987; *Barnett et al.*, 1990]	In accordance to *Chanteur et al.* [2009] σ_{20} was taken equal to 2.5 × 10^{-16} cm^2 for $E < 5$ keV.
4. Ionization: He^{2+} + M → He^{2+} + M+ + e			
4.1	He^{2+} + CO$_2$	Not available	Based on H$^+$ + CO$_2$ from *Haider et al.* [2002] with the scaling factor the same as for He^{2+} + O.
4.2	He^{2+} + N$_2$	Not available	Based on H$^+$ + N$_2$ from *Haider et al.* [2002].
4.3	He^{2+} + O	Not available	Based on H$^+$ + O from *Haider et al.* [2002] normalized by the factor 0.5 to match the calculated cross-section for He^{2+} + O at 10 keV [*Sahoo*, 2000].
4.4-6	He^{2+} + H, H$_2$, He	[*Ito et al.*, 1995]	σ_{io} (He^{2+} + H) is < 10^{-21} cm^2 for $E < 10$ keV
4.7-9	He$^+$ + CO$_2$ N$_2$, O	Not available	Same as for He^{2+} + CO$_2$, N$_2$, O
4.10-12	He$^+$ + H, H$_2$, He	[*Ito et al.*, 1995]	σ_{io} (He$^+$ + H) is < 10^{-20} cm^2 for $E < 10$ keV
4.13-14	He + H$_2$, He	[*Ito et al.*, 1995]	
4.15	He + H	Not available	Neglected
5. Stripping: He$^+$ + M → He^{2+} + M + e or He + M → He$^+$ + M + e			
5.1-3	He$^+$ + CO$_2$ N$_2$, O	Not available	Neglected in the model
5.4-6	He$^+$ + H, H$_2$, He	[*Ito et al.*, 1995]	Values of $\sigma_{12} < 10^{-21}$ cm^2 for $E < 10$ keV
5.7-9	He + CO$_2$ N$_2$, O	Not available	Neglected in the model
5.10-12	He + H, H$_2$, He	[*Ito et al.*, 1995]	Values of $\sigma_{01} < 10^{-21}$ cm^2 for $E < 10$ keV

[50]   3. For He$^+$, He^{2+} + CO$_2$, N$_2$, O, H, H$_2$, and He collisions, we did not find the measurements. Therefore, we use the same the SADs as for the He collisions with these neutral species.

References

Akalin, F., D. D. Morgan, D. A. Gurnett, D. L. Kirchner, D. A. Brain, R. Modolo, M. H. Acuna, and J. R. Espley (2010), Dayside induced magnetic field in the ionosphere of Mars, *Icarus*, *206*, 104–111.

Brain, D. A., F. Bagenal, M. H. Acuna, and J. E. P. Connerney (2003), Martian magnetic morphology: Contributions from the solar wind and crust, *J. Geophys. Res.*, *108*, 1424, doi:10.1029/2002JA009482.

Barabash, S., and O. Norberg (1994), Indirect detection of the Martian helium corona, *Geophys. Res. Lett.*, *21*, 1547–1550.

Barabash, S., E. Kallio, R. Lundin, and H. Koskinen (1995), Measurements of the nonthermal helium escape from Mars, *J. Geophys. Res.*, *100*, 21,307–21,316.

Barabash, S., et al. (2006), The analyzer of space plasmas and energetic atoms (ASPERA-3) for the Mars Express mission, *Space Sci. Rev.*, *126*, 1–4, 113–164.

Barnett, C. F., H. T. Hunter, M. I. Fitzpatrick, I. Alvarez, C. Cisneros, and R. A. Phaneuf (1990), Atomic data for fusion. Volume 1: Collisions of H, H2, He and Li atoms and ions with atoms and molecules, NASA STI/Recon Technical Report, *91*, 13238.

Bisikalo, D. V., V. I. Shematovich, and J.-C. Gérard (1995), Kinetic model of the formation of the hot oxygen geocorona. II. Influence of O$^+$ ion precipitation, *J. Geophys. Res.*, *100*, 3715–3720.

Bretch, S. H.(1997), Hybrid simulations of the magnetic topology of Mars, *J. Geophys. Res.*, *102*, 4743-4750

Bovino, S., P. Zhang, F. A. Gianturco, A. Dalgarno, and V. Kharchenko (2011), Energy transfer in O collisions with He isotopes and Helium escape from Mars, *Geophys. Res. Lett.*, *38*, L02203, doi:10.1029/2010GL045763.

Chanteur, G. M., E. Dubinin, R. Modolo, and M. Fraenz (2009), Capture of solar wind alpha-particles by the Martian atmosphere, *Geophys. Res. Lett.*, *36*, doi:10.1029/2009GL040235.

Diéval C., et al. (2012), A case study of proton precipitation at Mars: Mars Express observations and hybrid simulations, *J. Geophys. Res.*, *117*, A06222, doi:10.1029/2012JA017537.

Fox, J. L., and A. B. Hac (2009), Photochemical escape of oxygen from Mars: A comparison of the exobase approximation to a Monte Carlo method, *Icarus*, *204*, 527–544.

Gao, R. S., L. K. Johnson, C. L. Hakes, K. A. Smith, and R. F. Stebbings (1990), Collisions of kilo-electron-volt H+ and He+ with molecules at small angles: Absolute differential cross sections for charge transfer, *Phys. Rev. A*, *41*, 5929.

Gao R. S., L. K. Johnson, D. A. Schafer, J. H. Newman, K. A. Smith, and R. F. Stebbings (1988), Absolute differential cross sections for small-angle He$^+$- He elastic and charge-transfer scattering at keV energies, *Phys. Rev. A*, *38*, 2789.

Gérard J.-C., B. Hubert, D. V. Bisikalo, and V. I. Shematovich (2000), A model of the Lyman-α line profile in the proton aurora, *J. Geophys. Res.*, *105*, 15795–15806.

Haider, S. A., S. P. Seth, E. Kallio, and K. I. Oyama (2002), Solar EUV and electron-proton-hydrogen atom-produced ionosphere on Mars: Comparative studies of particle fluxes and ion production rates due to different processes, *Icarus*, *159*, 18–30.

Ito R., T. Tabata, T. Shirai, and R. A. Phaneuf (1993), Analytic Cross Sections for Collisions of H, H2, He and Li Atoms and Ions Colliding with Atoms and Molecules. I, *JAERI-M*, 93–117.

Ito R., T. Tabata, T. Shirai, and R. A. Phaneuf (1995), Analytic Cross Sections for Collisions of H, H2, He and Li Atoms and Ions Colliding with Atoms and Molecules. III, *JAERI-Data/Code* 95-008.

Janev, R. K., W. D. Langer, and K. Evans (1987), Elementary processes in Hydrogen-Helium plasmas - Cross sections and reaction rate coefficients, Springer Series on Atoms and Plasmas, Springer, Berlin.

Kallio, E., and S. Barabash (2001), Atmospheric effects of precipitating energetic hydrogen atoms on the Martian atmosphere, *J. Geophys. Res.*, *106*, 165–178.

Krasnopolsky, V. A., and G. R. Gladstone (2005), Helium on Mars and Venus: EUVE observations and modeling, *Icarus*, *176*, 395–407.

Krasnopolsky, V. A., S. Chakrabarti, and G. R. Gladstone (1993), Helium in the Martian atmosphere, *J. Geophys. Res.*, *98*, 15,061–15,068.

Krasnopolsky, V. A., S. Bowyer, S. Chakrabarti, G. R. Gladstone, and J. S. McDonald (1994), First measurements of helium on Mars: Implications for the problem of radiogenic gases on the terrestrial planets, *Icarus*, *109*, 337–351.

Krstić, P. S., and D. R. Schultz (2006), Elastic and related transport cross sections for protons scattering from the noble gases He, Ne, Ar, Kr, and Xe, *Physics of Plasmas*, *13*, 053501-0535019-9.

Kusakabe T., Y. Miyamoto, M. Kimura, and H. Tawara (2006), Charge-transfer processes in collisions of He2+ ions with H2, N2, O2, CO, and CO2 molecules below 4 keV/u, *Phys. Rev. A*, *73*, 022706.

Lindsay, B. G., and R. F. Stebbings (2005), Charge transfer cross sections for energetic neutral atom data analysis, *J. Geophys. Res.*, *110*, A12213, doi:10.1029/2005JA011298.

Lundin, R., et al. (2004), Solar wind-induced atmospheric erosion at Mars: first results from ASPERA-3 on Mars Express, *Science*, *305*(5692), 1933–1936, doi:10.1126/science.1101860.

Modolo, R., G. M. Chanteur, E. Dubinin, A. P. Matthews (2005), Influence of the solar EUV flux on the Martian plasma environment, *Annales Geophysicae*, *23*, 433-444

Modolo, R., G. M. Chanteur, Y. Futaana, S. Barabash, E. Dubinin, and A. P. Matthews (2005), Influence of the solar EUV flux on the Martian plasma environment, *Annales Geophysicae*, *23*, 433-444.

Nagy, A. F., et al. (2004), The plasma environment of Mars, *Space Sci. Rev.*, *111*, 33–114, doi:10.1023/B:SPAC.0000032718.47512.92.

Newman, J. H., K. A. Smith, and R. F. Stebbings (1985), Differential scattering cross sections for collisions of 0.5-, 1.5-, and 5.0- keV helium atoms with He, H2, N2, and O2, *J. Geophys. Res.*, *90*, 11,045–11,054.

Sahoo S. (2000), Ionization of atomic oxygen in collision with proton and alpha particle, *Phys. Scr.*, *62*, 145–147.

Shematovich, V. I. (2008), Kinetics of suprathermal atoms and molecules in the rarefied planetary atmospheres, In RARIFIED GAS DYNAMICS: Proceedings of the 26th International Symposium on Rarefied Gas Dynamics. *AIP Conference Proceedings*, *1084*, 1047–1054.

Shematovich, V. I., D. V. Bisikalo, and J.-C. Gérard (1994), A kinetic model of the formation of the hot oxygen geocorona. I. Quiet geomagnetic conditions, *J. Geophys. Res.*, *99*, 23217–23228.

Shematovich V. I., D. V. Bisikalo, C. Diéval, S. Barabash, G. Stenberg, H. Nilsson, Y. Futaana, M. Holmstrom, and J.-C. Gérard, Proton and hydrogen atom transport in the Martian upper atmosphere with an induced magnetic field, *J. Geophys. Res.*, 116, 2011, doi:10.1029/2011JA017007

Rudd, M. E., Goffe, T. V., and A. Itoh (1985), Ionization cross sections for 10-300-keV/u and electron-capture cross sections for 5-150-keV/u ^{3}He^{2+} ions in gases, *Phys. Rev. A*, *32*, 2128–2133.

Stenberg, G., H. Nilsson, Y. Futaana, S. Barabash, A. Fedorov, and D. Brain (2011), Observational evidence of alpha-particle capture at Mars, *Geophys. Rev. Lett.*, *38*, L09101, doi:10.1029/2011GL047155.